ACS APPLIED MATERIALS & INTERFACES

Research Article

Cite This: ACS Appl. Mater. Interfaces 2019, 11, 22979−22986

www.acsami.org

Magnetic Nanoparticle Relaxation Dynamics-Based Magnetic Particle Spectroscopy for Rapid and Wash-Free Molecular Sensing

Kai Wu,*[,†] Jinming Liu,[†] Diqing Su,[‡] Renata Saha,[†] and Jian-Ping Wang*[,†]

[†]Department of Electrical and Computer Engineering and [‡]Department of Chemical Engineering and Material Science, University of Minnesota, Minneapolis, Minnesota 55455, United States

Supporting Information

ABSTRACT: Magnetic nanoparticles (MNPs) have been extensively used as contrasts and tracers for bioimaging, heating sources for tumor therapy, carriers for controlled drug delivery, and labels for magnetic immunoassays. Here, we describe a MNP Brownian relaxation dynamics-based magnetic particle spectroscopy (MPS) method for the quantitative detection of molecular biomarkers. In MPS measurements, the harmonics of oscillating MNPs are recorded and used as a metric for the freedom of rotational motion, which indicates the bound states of the MNPs. These harmonics can be collected from microgram quantities of iron oxide nanoparticles within 10 s. As the harmonics are largely dependent on the quantity of the MNPs in the sample, the MPS bioassay results could be biased by the deviations of MNP quantities in each sample, especially for the very low-concentration biomarker detection scenarios. Herein, we report three MNP concentration/quantity-independent metrics for characterizing the bound states of MNPs in MPS. Using a streptavidin−biotin binding system as a model, we demonstrate the feasibility of using MPS and MNP concentration/quantity-independent metrics to sense these molecular interactions, showing that this method can achieve rapid, wash-free bioassays, and is suitable for future point-of-care, sensitive, and versatile diagnosis.

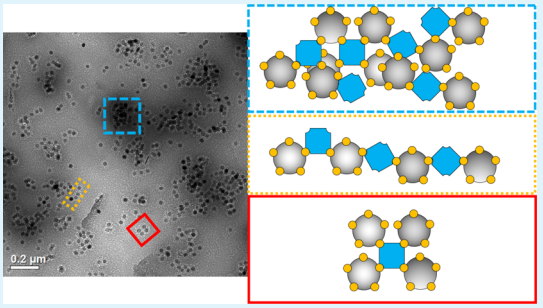

KEYWORDS: *magnetic nanoparticle, magnetic particle spectroscopy, Brownian relaxation, wash-free, point-of-care, bioassay*

1. INTRODUCTION

In recent years, magnetic nanoparticles (MNPs) have been successfully applied as nano-heaters for hyperthermia therapy, nano-carriers for drug delivery, nano-tracers for magnetic particle imaging (MPI), nano-contrast agents for magnetic resonance imaging, and nano-labels for magnetic bioassays.[1−27] MNPs, with physical size comparable to biologically important substances, have many unique physicochemical properties such as high surface to volume ratio and size-dependent magnetic properties, making them ideal for many novel applications. Nowadays, MNPs with a properly functionalized surface can be physically and chemically stable, biocompatible, and environmentally friendly.[28] Furthermore, biological samples exhibit virtually no magnetic background; thus, high-sensitivity measurements can be performed on minimally processed samples in MNP-based biomedical applications. In addition, the ease of synthesis and facile surface chemistry have generated much eagerness in applying MNPs to clinical diagnostics and therapy.

Magnetic particle spectroscopy (MPS) is a novel measurement method that closely relates to MPI, which has been widely explored by many groups in recent years.[29−41] In MPS, sinusoidal magnetic fields periodically drive MNPs into magnetically saturated regions which generate magnetic responses that contain not only the drive field frequencies but also a series of harmonic frequencies. These harmonic components can be easily extracted by filtering and fast Fourier transform. The harmonics are very useful metrics of the MNP ferrofluids which contain important information such as the viscosity and temperature of the MNP solution as well as the conjugation of any ligands/chemicals onto MNPs.[30,42−50] It has been reported that as the harmonic amplitude is largely dependent on the quantity of the MNPs in the sample, the MPS bioassay results could be biased by the deviations of MNP quantities in each sample, especially for the very low-concentration biomarker detection scenarios.[30,30,34] Because of this concern, it has been reported that magnetic susceptibility is MNP quantity-independent for MNP-based immunoassays.[51−53] Herein, we are reporting three MNP concentration/quantity-independent metrics for characterizing the bound states of MNPs in MPS, namely, the $f_{H,crit}$ at peak harmonic amplitude (unit: Hz), 1/2 fwhm (unit: Hz), and the ratios of the 3rd to the 5th harmonics (R35). We used a MNP Brownian relaxation dynamics-based MPS method as the model for the rapid and wash-free molecular sensing. This type of measurement relies on the fact that the tendency of MNPs' magnetic moments to align with the external magnetic field is countered by the Brownian relaxation that randomizes the MNPs' alignment. The extent of disorder caused by Brownian relaxation is most sensitive to the bound state of MNPs,

Received: March 27, 2019
Accepted: June 6, 2019
Published: June 6, 2019

DOI: 10.1021/acsami.9b05233
ACS Appl. Mater. Interfaces 2019, 11, 22979−22986

namely, the hydrodynamic size. The higher harmonics (the 3rd and 5th harmonics) are extracted from the MPS for analyzing the bound states of MNPs.

We verified the feasibility of using these MNP concentration/quantity-independent metrics in MNP Brownian relaxation-based MPS molecular sensing. The well-characterized streptavidin and biotin system with ultrahigh binding affinity is chosen as the model system, demonstrating the validity of MPS and MNP concentration/quantity-independent metrics for future rapid, point-of-care (POC), sensitive, and versatile immunoassays. The results show that the MNP Brownian relaxation-based MPS method can detect analytes directly from biological samples with minimum sample preparation in a wash-free manner.

2. MATERIALS AND METHODS

2.1. Materials. The MNPs used in this work are iron oxide nanoparticles (IONPs) with average core size of 30 nm and coated with a layer of biotin, purchased from Ocean NanoTech, San Diego, California (catalog no. SHB-30). The streptavidin from *Streptomyces avidinii* is a salt-free, lyophilized powder with biotin-binding capacity of 13 units/mg protein, purchased from Sigma-Aldrich Inc., Atlanta, Georgia (product no. S4762). Phosphate-buffered saline (PBS) is purchased from Sigma-Aldrich Inc., Atlanta, Georgia (product no. 79378).

2.2. Sample Preparation. The lyophilized streptavidin powder is reconstituted in PBS and prepared with different concentrations varying from 75 nM to 15 μM. As shown in Scheme 1, six samples

Scheme 1. Composition of Six MNP Samples

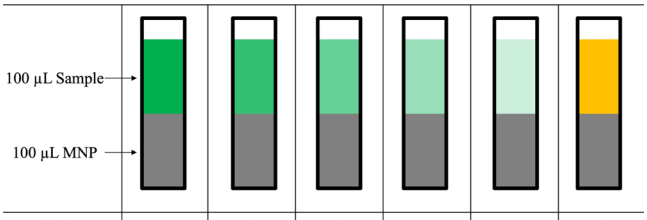

Vial #	I	II	III	IV	V	VI
Streptavidin Concentration	15 μM	7.5 μM	3.8 μM	1.5 μM	75 nM	0 (PBS)

(vial I–VI) are prepared and each sample contains approximately 100 μL of MNPs. Vials I–V are active groups and each vial is added with 100 μL of streptavidin of different concentrations. Vial VI serves as the control group and it is added with 100 μL of PBS. All the samples are mixed well and incubated at room temperature for 30 min to allow the binding of streptavidin to biotins from the MNPs.

2.3. Conjugation of Streptavidin to MNPs. Streptavidin is a crystalline tetrameric protein, with a molecular weight of 4 × 15 kDa. It binds four molecules of biotin and has a high binding affinity to biotin ligands (dissociation constant $K_d = 10^{-14}$ M). The binding between biotin and streptavidin is very fast, and once formed, it is independent of temperature, solvents, pH, and other denaturing agents. Each streptavidin hosts four biotin binding sites, which allows the interaction with multiple biotin moieties from different MNPs and, as a result, forms MNP clusters.

2.4. Experimental Setups. The MPS measurement system setups and signal chain are shown in Figure 1a,b. A personal computer controls the data acquisition card (DAQ, NI USB-6289) to generate two sinusoidal signals, which are amplified by two instrument amplifiers (IA, HP 6824A), followed by two band pass filters (BPFs) to suppress higher harmonics that might be introduced by IAs. These amplified and filtered sinusoidal signals drive the outer and inner coils (see Figure 1c,d) to generate oscillating magnetic fields: one with frequency f_L = 10 Hz and amplitude A_L = 170 Oe, the other with frequency f_H that varies from 500 Hz to 20 kHz and amplitude A_H = 17 Oe. One pair of differentially wound pick-up coils (600 windings clock-wise and 600 windings counter-clock-wise) collect the induced voltage and phase signals from MNPs and send them back to a BPF before digitalizing on the DAQ. The response signals at combinatorial frequencies $f_H \pm 2f_L$ (3rd harmonic) and $f_H \pm 4f_L$ (5th harmonic) are analyzed.

2.5. Molecular Sensing via MPS. When the single-domain MNPs are suspended in solution and subjected to an external magnetic field, there are two mechanisms by which the magnetic moments rotate in response to the magnetic field (see Scheme 2a,b): the intrinsic Néel motion (rotating magnetic moment inside a stationary particle) and the extrinsic Brownian motion (rotating the entire particle along with its magnetic moment). In principle, both the Néel and Brownian mechanism play a role in determining the magnetization of MNP ferrofluids subjected to external oscillating magnetic fields.[32] In this work, we use MNPs with core size of 30 nm, where the Brownian mechanism is dominant and the Néel mechanism is minimized. For these Brownian-relaxation-dominated MNPs, their MPS responses are most sensitive to the hydrodynamic sizes of MNPs. As shown in Scheme 2c,d, when the target biomarker (i.e., streptavidin) has multiple binding sites, ligands (i.e., biotins) from more than one MNP can bind to the same biomarker, resulting in the clustering of MNPs. Such an interaction greatly increases the hydrodynamic sizes of MNPs as well as the Brownian relaxation time. As a result, noticeable changes could be found from the MPS responses because of this specific binding process. Mathematical models of the relaxation mechanisms can be found in Notes S1 and S2 in the Supporting Information.

3. RESULTS AND DISCUSSIONS

3.1. MPS Characterization of Magnetic Relaxation Dynamics. The MPS response upon increasing streptavidin concentrations from 75 nM to 15 μM is investigated, and one control group is added in this experiment to verify this detection strategy: biotin-coated MNPs with the addition of PBS. The frequency of high-frequency drive field f_H is varied at 500 Hz, 1 kHz, 2 kHz, 4 kHz, 6 kHz, 8 kHz, 10 kHz, 12 kHz, 14 kHz, 16 kHz, 18 kHz, and 20 kHz, and the frequency of the low-frequency drive field f_L is set at 10 Hz. The amplitudes of both high- and low-frequency drive fields are identical in each test. During each test, the background noise is monitored for 10 s, then the plastic vial containing 200 μL sample is inserted into the pick-up coils, and followed by another 10 s of data collection on the total signal. Some examples of the real-time magnetic responses sensed by pick-up coils are shown in Note S8 in the Supporting Information. The MPS response of MNPs is extracted by subtracting the background noise from the total signal using the phasor theory we reported before[37,54,55]

$$A_{MNP}\, e^{j\varphi_{MNP}}|_m = A_{TOT}\, e^{j\varphi_{TOT}}|_m - A_{noise}\, e^{j\varphi_{noise}}|_m \quad (1)$$

where A_{MNP}, A_{TOT}, A_{noise} are the amplitudes from MNPs, total signal, and the background noise, respectively, and φ_{MNP}, φ_{TOT}, and φ_{noise} are the phase angles from MNPs, total signal, and the background noise, respectively, m represents the mth measured harmonic. The phasor model can be found in Note S4 in the Supporting Information.

The 3rd and 5th harmonic amplitudes of MNPs from six samples are reconstructed from the total signals and background noise. They are summarized in Figure 2a,c. According to the Debye model and Faraday's law of induction (mathematical models of the MPS responses can be found in Notes S3–S5 in the Supporting Information), the harmonic amplitude is dependent on the drive field frequency f_H, the

DOI: 10.1021/acsami.9b05233
ACS Appl. Mater. Interfaces 2019, 11, 22979–22986

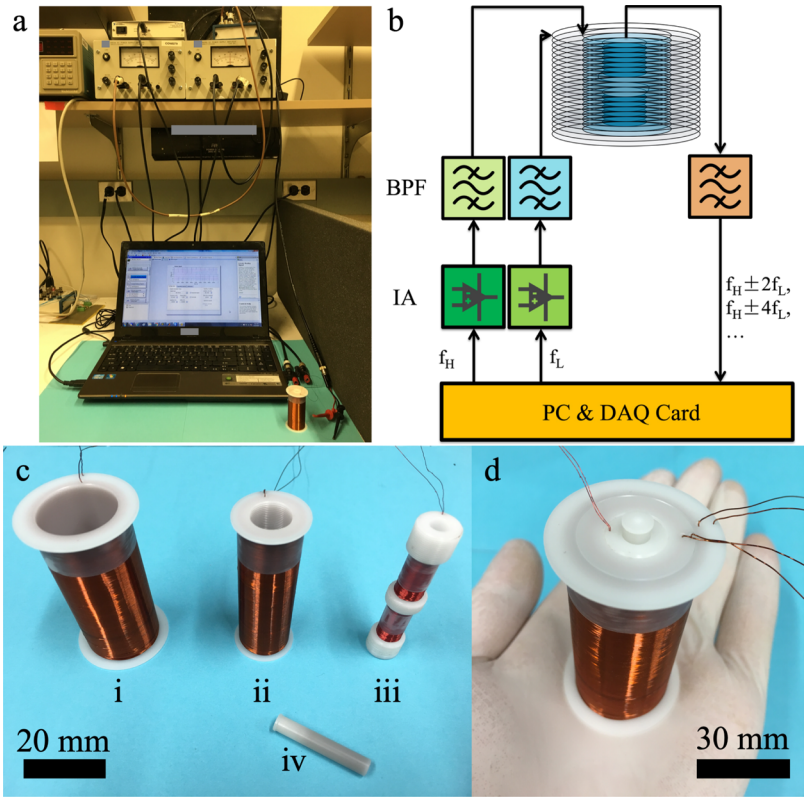

Figure 1. MPS measurement system setups. (a) Photograph of system setups. (b) Signal chain. The system used in this work records nonlinear magnetic response of MNPs under two oscillating magnetic fields with frequencies of f_H and f_L. (c) Photograph of coils: (i) low-frequency drive coil (outer coil); (ii) high-frequency drive coil (inner coil); (iii) a pair of pick-up coils; (iv) plastic vial with a capacity of 300 μL. (d) Photograph of the assembled coils.

Scheme 2. (a) Néel Relaxation is the Rotation of a Magnetic Moment Inside a Stationary MNP; (b) Brownian Relaxation is the Rotation of the Entire MNP along with the Magnetic Moment; (c) tStreptavidin Has a High Binding Affinity to the Biotin Ligands on the MNP Surface; (d) as the Quantity of Streptavidin Increases in the MNP Suspension, the MNPs are Likely to Form Clusters; the Dashed Lines Represent the Hydrodynamic Sizes of MNPs Because of the Clustering Induced by Streptavidin; as the MNP Clustering Level Increases, the Hydrodynamic Size Increases, and the Harmonic Amplitude Decreases

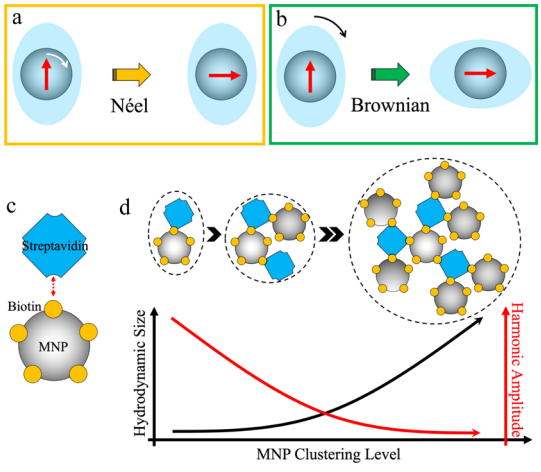

cosine of phase lag φ, and the quantity of MNPs in the testing sample. The increased streptavidin concentration/quantity in the MNP sample causes larger MNP clusters. The hydrodynamic sizes as well as the phase lags of the MNPs increase, which, as a result, causes a noticeable drop in harmonic amplitudes (see Scheme 2d). As shown in Figure 2a,c, the harmonic amplitudes of the 3rd and 5th harmonics decrease as we increase the concentration/quantity of streptavidin in the MNP sample. However, the harmonic amplitudes from vial V (75 nM) are larger than those of the control sample, which is due to the deviations of MNP quantities in each sample. As the harmonic amplitude is largely dependent on the quantity of the MNPs from the sample, the testing results could be biased by the deviations of MNP quantities in each sample, especially for the very low-concentration biomarker detection scenarios. Thus, in this paper, we used the MNP quantity-independent metrics: the normalized 3rd and 5th harmonics and the ratios of the 3rd to the 5th harmonics (R35) to quantify the concentrations of the target biomarker.

First, we report here the normalized 3rd and 5th harmonics as a MNP quantity-independent metric for biomarker detection, which are plotted in Figure 2b,d. The dotted lines represent the critical frequencies $f_{H,crit}$ where the harmonic amplitudes reach peaks for the six MNP samples. There is a clear trend of the peaks moving to lower f_H for samples with higher concentrations/quantities of streptavidin (explained in Note S9 in the Supporting Information). As summarized in Table 1, the $f_{H,crit}$ at the peak harmonic amplitude decreases as the biomarker concentrations/quantities increase.

The insets in Figure 2b,d highlight the normalized 3rd and 5th harmonic amplitudes measured at 500 Hz and 10 kHz, respectively. We compared the normalized amplitude values

DOI: 10.1021/acsami.9b05233
ACS Appl. Mater. Interfaces 2019, 11, 22979−22986

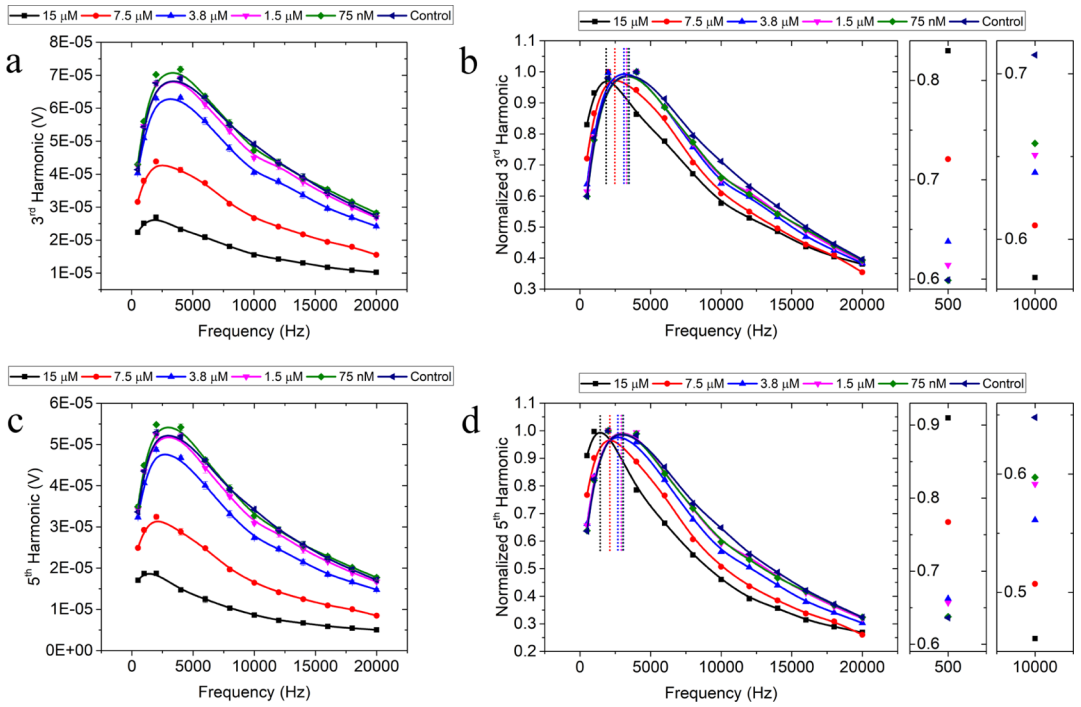

Figure 2. (a,c) MPS measurements of the 3rd and 5th harmonics from six MNP samples in different bound states. The error bar represents standard deviation. (b,d) MPS measurements of the normalized 3rd and 5th harmonics from six MNP samples in different bound states. The insets in (b,d) highlight the normalized harmonic amplitudes measured at 500 Hz and 10 kHz, respectively. The dotted line represents the position of the peak harmonic signal for each sample as the drive field frequency varies.

Table 1. Summarized Peak Shift of Harmonic Signals and 1/2 fwhm from Six MNP Samples

vial #	I (15 μM)	II (7.5 μM)	III (3.8 μM)	IV (1.5 μM)	V (75 nM)	VI (0 nM)
$f_{H,crit}$ at peak harmonic amplitude (Hz)	2000	2500	2700	2800	2850	2900
1/2 fwhm[a] (Hz)	11 300	11 800	12 300	12 700	12 900	13 100

[a]1/2 fwhm is the difference between $f_{H,crit}$ at the peak harmonic amplitude and $f_{H,50\%}$ at 50% of the peak harmonic amplitude.

from six MNP samples before and after the onset of the peaks. It is found that before the onset of the peaks (at 500 Hz), the measured normalized harmonic amplitudes arranged from highest to lowest are: I (15 μM) > II (7.5 μM) > III (3.8 μM) > IV (1.5 μM) > V (75 nM) > VI (control, 0 nM). However, after the onset of the peaks (at 10 kHz), the measured normalized harmonic amplitudes reversed, namely, from highest to lowest are: VI (control, 0 nM) > V (75 nM) > IV (1.5 μM) > III (3.8 μM) > II (7.5 μM) > I (15 μM), which indicates that the peak widths from the normalized 3rd and 5th harmonic curves vary for six MNP samples in different bound states. In view of this, we introduce the full width at half-maximum (fwhm) as another MNP quantity-independent metric for characterizing the biomarker concentrations/quantities from MNP samples. As the normalized harmonic amplitude curves in Figure 2b,d are not full-pulse waveforms, we use 1/2 fwhm, which is the difference between $f_{H,crit}$ at the peak harmonic amplitude and $f_{H,50\%}$ at 50% of the peak harmonic amplitude. It is observed from Figure 2b,d that the 1/2 fwhm decreases as the concentrations/quantities of streptavidin increases in the MNP sample. In other words, the normalized harmonic amplitude curve is steeper from MNP samples with higher concentrations/quantities of biomarkers. As summarized in Table 1, the 1/2 fwhm value increases as the biomarker concentrations/quantities increases.

To the best of our knowledge, it is for the first time that $f_{H,crit}$ at the peak harmonic amplitude and 1/2 fwhm as MNP quantity-independent metrics are being used for characterizing the biomarker concentrations/quantities.

On the other hand, the ratios of the 3rd to the 5th harmonics (R35) at different drive field frequencies have also been used as a MNP quantity-independent metric for characterizing the biomarker concentrations/quantities from samples (the harmonic ratio model can be found in Note S6 in the Supporting Information). Figure 3a summarizes the harmonic ratios, R35, from six samples as we vary the drive field frequency f_H from 500 Hz to 20 kHz. The harmonic ratios R35 increase as the concentrations/quantities of streptavidin increases. The inset figure in Figure 3a lists the harmonic ratios R35 from six samples at a drive field frequency of f_H = 10 kHz. The R35 drops from 1.7978 for sample I (streptavidin concentrations: 15 μM) to 1.4332 for sample VI (streptavidin concentrations: 0 nM). Figure 3b–e shows the relationships between R35 and streptavidin concentrations under different drive field frequencies. It is noted that the harmonic ratio R35 increases as the concentrations/quantities of streptavidin increases in the MNP sample. Under low drive field frequency, f_H = 500 Hz (Figure 3b), the difference in R35 between samples I (streptavidin concentrations: 15 μM) and VI (streptavidin concentrations: 0 nM) is only 6%. On the other hand, under high drive field frequency, f_H = 18 kHz (Figure 3e), this difference reaches 28%. Hence, the harmonic ratio, R35, under higher drive field frequency allows for better

DOI: 10.1021/acsami.9b05233
ACS Appl. Mater. Interfaces 2019, 11, 22979–22986

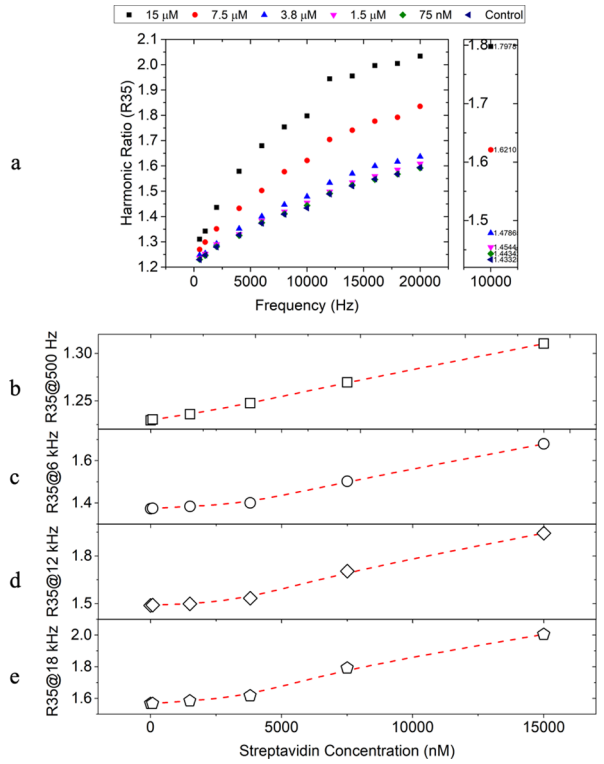

Figure 3. MPS measurements of the ratio of the 3rd to the 5th harmonics (R35) of six MNP samples in different bound states. (a) Harmonic ratios, R35, from six samples as we vary the f_H from 500 Hz to 20 kHz. The inset figure summarizes the R35 under a drive field frequency of f_H = 10 kHz for vials I–VI, the R35 values are: 1.7978 (15 μM), 1.6210 (7.5 μM), 1.4786 (3.8 μM), 1.4544 (1.5 μM), 1.4434 (75 nM), and 1.4332 (control, 0 nM), respectively. (b–d) Relationships between R35 and streptavidin concentrations at drive field frequencies of (b) 500 Hz; (c) 6 kHz; (d) 12 kHz; and (e) 18 kHz.

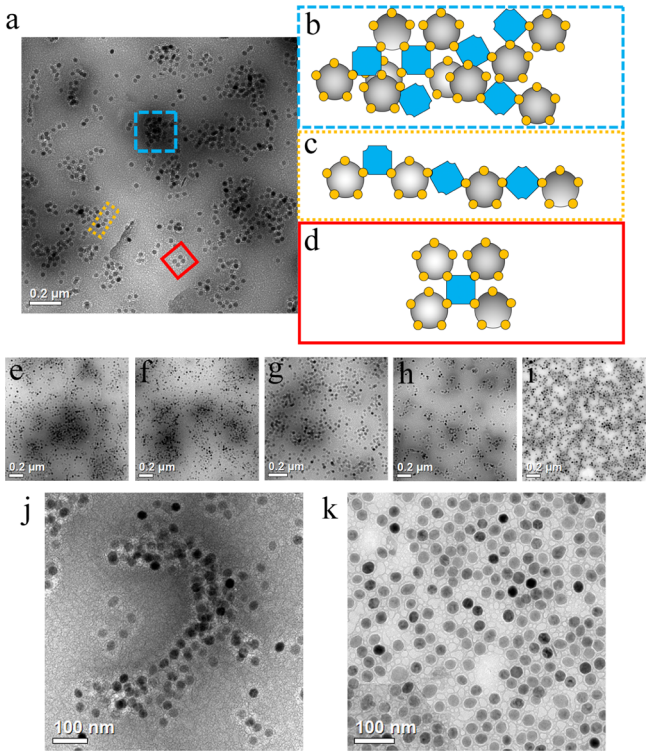

Figure 4. Bright-field TEM images of six MNP samples in different bound states. (a) Ssample I (15 μM) showing different MNP bound states. (b) MNP cluster model representing the blue dashed contour in (a). (c) MNP chain model representing the orange dotted contour in (a). (d) MNP tetramer model representing the red solid contour in (a). Blue square represents streptavidin, orange dot represents biotin, and gray circle represents MNP. (e–i) Samples I (15 μM), II (7.5 μM), III (3.8 μM), V (75 nM), and VI (0 nM) showing that the cluster size increases as the number of streptavidin increases. (j,k) Comparison of samples I (15 μM) and VI (0 nM) showing one of the MNP clusters in the presence of streptavidin and the well-dispersed MNPs in the absence of streptavidin.

resolutions in characterizing the target biomarker concentrations.

Besides the peak shift, 1/2 fwhm, and harmonic ratio (R35) methods, the harmonic angle is also a MNP concentration/quantity-independent metric for characterizing the bound states of MNPs in MPS.[46] The 3rd and the 5th harmonic angles are reconstructed from the total signals and background noise. They are summarized in Note S7 in the Supporting Information.

3.2. Morphological Characterization of MNPs in Different Bound States. Transmission electron microscopy (TEM) images are taken to investigate the MNP clusters and bound states in six samples after the MPS measurements. A droplet of the MNP solution (~10 μL) is dropped onto a TEM grid (copper mesh with amorphous carbon film) with filter paper underneath. The MNP droplet forms a thin liquid layer on the TEM grid and will be ready for TEM characterization when the solution evaporates. Then, the TEM grids are characterized in TEM (FEI Tecnai T12, 120 kV). Well-dispersed MNPs are observed from the control sample without streptavidin (vial VI, 0 nM) as seen in Figure 4i,k whereas more MNP clusters could be found with the increase of streptavidin concentrations. As shown in Figure 4e–i, an increased streptavidin concentration produces larger MNP clusters as observed in TEM images. Figure 4a shows different bound states of MNPs in the presence of streptavidin. As there are multiple biotins on each MNP and the tetrameric structure of streptavidin hosting four biotin bindings sites, MNPs could form clusters, chains, tetramers, trimers, dimers, and so forth. Figure 4b–d shows the corresponding models of MNP bound states from Figure 4a. Figure 4j,k is the zoomed-in views of one "~-shape" MNP cluster from vial I and the well-dispersed MNPs from vial VI.

3.3. Hydrodynamic Size Analysis of MNPs in Different Bound States. Dynamic light scattering (DLS) measurements confirmed the streptavidin-specific clustering and the hydrodynamic size increased with streptavidin concentration. Statistic results from Figure 5 give us the mean hydrodynamic sizes of vials I–VI: 706, 102.8, 63.2, 58.8, 58.4, and 58.3 nm, respectively. The results from DLS are in good agreement with our MPS and TEM measurements.

4. CONCLUSIONS AND FUTURE PERSPECTIVES

In this work, we have demonstrated the feasibility of using a MNP relaxation dynamics-based MPS method for bioassay applications. The specific binding of target analytes onto a MNP surface inhibits their rotational freedom, and thus changes the MPS pattern. The streptavidin and biotin systems are applied in this study as a model system. Each streptavidin has binding sites for multiple MNPs and forms MNP clusters

DOI: 10.1021/acsami.9b05233
ACS Appl. Mater. Interfaces 2019, 11, 22979–22986

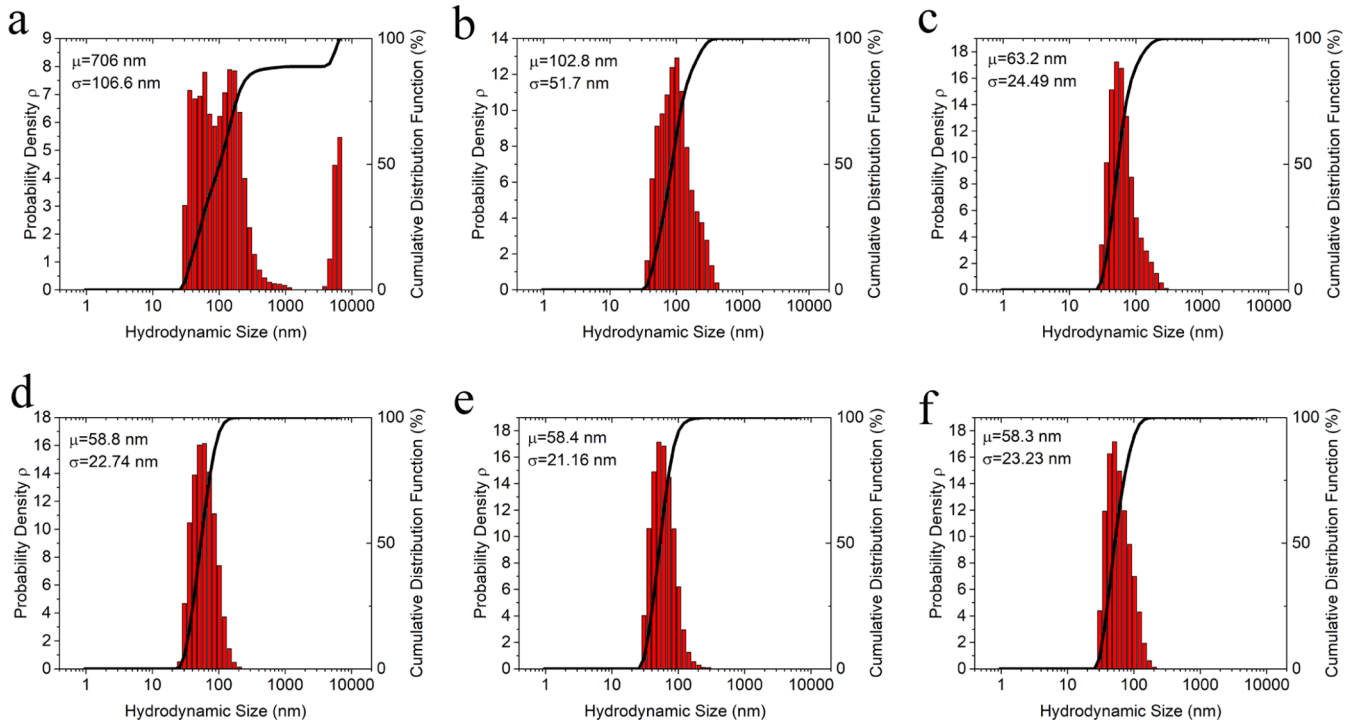

Figure 5. Statistical hydrodynamic size distribution collected using DLS. (a–f) Vials I–VI. Solid black lines are cumulative distribution curves; μ and σ denote the mean and the standard deviation of hydrodynamic sizes.

that tremendously increase the hydrodynamic sizes of MNPs. As a result, noticeable changes could be found in the harmonic phase lags and amplitudes. Herein, we have reported three MNP concentration/quantity-independent metrics for characterizing the bound states of MNPs in MPS, namely, the $f_{H,crit}$ at peak harmonic amplitude (unit: Hz), 1/2 fwhm (unit: Hz), and the ratios of the 3rd to the 5th harmonics (R35). The $f_{H,crit}$ at the peak harmonic amplitude and 1/2 fwhm metrics require the full screening of drive field frequency f_H from several hundred of Hz to several tens' kHz (in this work we varied f_H from 500 Hz to 20 kHz). Although it is time-consuming to collect the MPS responses under varying drive field frequencies, $f_{H,crit}$ and 1/2 fwhm metrics can provide high-sensitivity bioassays if f_H is varied with a small step width (i.e., better frequency resolution). On the other hand, the harmonic ratio R35 provides an alternative way to carry out faster MPS bioassay measurements as it does not require the full screening of the drive field frequencies. As shown in Figure 3b–e, it is possible to collect the R35 under one drive field frequency and use this metric to characterize the target biomarker concentration/quantity. However, the harmonic ratio R35 is unable to provide very high sensitivity bioassays compared to $f_{H,crit}$ and 1/2 fwhm metrics because of the factor that R35 from MNP samples with very low biomarker concentrations are very close to the control sample and it is susceptible to the system noise from MPS and the environmental noise. Although these subtle differences in the R35 from MNP samples with very low biomarker concentrations might be ruined by the noise, it is possible to avoid this issue by using a more accurate MPS system with lower system noise and carrying out the measurements in a magnetic shielding room. In addition, it is worthwhile to mention that all the three MNP concentration/quantity-independent metrics we reported in this work are temperature-dependent. Thus, the MPS measurements should be carried out under the same testing temperature to reduce the variances between different MPS-based bioassays.

The MNP concentration/quantity-independent metrics used in this work achieved a sensitivity of 75 nM for the detection of streptavidin using our MPS system (7.5 pmol streptavidin). There are several advantages in this MPS method: wash-free and easy-to-use bioassay (measurements could be carried out on minimally processed biological samples by non-technicians with minimum training requirements), rapid (the testing time is within 10 s), cheap (the cost for each trail only requires microgram quantities of IONPs), and portable (the coils, amplifiers, filters, and DAQ could be assembled onto a single PCB board).

Future development in this MNP relaxation dynamics-based bioassay method is to improve the sensitivity of MPS measurements as well as increase the signal-to-noise ratio. In summary, this MNP relaxation dynamics-based MPS method for bioassay applications opens a door for future POC, versatile, sensitive, rapid, and wash-free molecular sensing.

■ ASSOCIATED CONTENT

Supporting Information

The Supporting Information is available free of charge on the ACS Publications website at DOI: 10.1021/acsami.9b05233.

Langevin model of magnetic response; Néel and Brownian relaxation models; phase lag model; phasor theory; induced signal model; harmonic ratio model; MPS measurements of harmonic angles; recorded real-time magnetic response from pick-up coils; and the normalized third and fifth harmonics as a MNP quantity-independent metric for biomarker detection (PDF)

DOI: 10.1021/acsami.9b05233
ACS Appl. Mater. Interfaces 2019, 11, 22979–22986

AUTHOR INFORMATION

Corresponding Authors

*E-mail: wuxx0803@umn.edu (K.W.).
*E-mail: jpwang@umn.edu (J.-P.W.).

ORCID

Kai Wu: 0000-0002-9444-6112
Jinming Liu: 0000-0002-4313-5816
Diqing Su: 0000-0002-5790-8744

Notes

The authors declare no competing financial interest.

ACKNOWLEDGMENTS

Portions of this work were conducted in the Minnesota Nano Center, which is supported by the National Science Foundation through the National Nano Coordinated Infrastructure Network (NNCI) under award number ECCS-1542202. Portions of this work were carried out in the Characterization Facility, University of Minnesota, a member of the NSF-funded Materials Research Facilities Network (www.mrfn.org) via the MRSEC program.

REFERENCES

(1) Chen, S.; Chiang, C.-l.; Hsieh, S. Simulating Physiological Conditions to Evaluate Nanoparticles for Magnetic Fluid Hyperthermia (MFH) Therapy Applications. *J. Magn. Magn. Mater.* **2010**, *322*, 247−252.

(2) Ovejero, J. G.; Cabrera, D.; Carrey, J.; Valdivielso, T.; Salas, G.; Teran, F. J. Effects of Inter-and Intra-Aggregate Magnetic Dipolar Interactions on the Magnetic Heating Efficiency of Iron Oxide Nanoparticles. *Phys. Chem. Chem. Phys.* **2016**, *18*, 10954−10963.

(3) Ruta, S.; Chantrell, R.; Hovorka, O. Unified Model of Hyperthermia via Hysteresis Heating in Systems of Interacting Magnetic Nanoparticles. *Sci. Rep.* **2015**, *5*, 9090.

(4) Yu, L.; Liu, J.; Wu, K.; Klein, T.; Jiang, Y.; Wang, J.-P. Evaluation of Hyperthermia of Magnetic Nanoparticles by Dehydrating DNA. *Sci. Rep.* **2014**, *4*, 7216.

(5) Kumar, C. S. S. R.; Mohammad, F. Magnetic Nanomaterials for Hyperthermia-Based Therapy and Controlled Drug Delivery. *Adv. Drug Deliv. Rev.* **2011**, *63*, 789−808.

(6) Ulbrich, K.; Holá, K.; Šubr, V.; Bakandritsos, A.; Tuček, J.; Zbořil, R. Targeted Drug Delivery with Polymers and Magnetic Nanoparticles: Covalent and Noncovalent Approaches, Release Control, and Clinical Studies. *Chem. Rev.* **2016**, *116*, 5338−5431.

(7) Huang, J.; Li, Y.; Orza, A.; Lu, Q.; Guo, P.; Wang, L.; Yang, L.; Mao, H. Magnetic Nanoparticle Facilitated Drug Delivery for Cancer Therapy with Targeted and Image-Guided Approaches. *Adv. Funct. Mater.* **2016**, *26*, 3818−3836.

(8) Rosengart, A. J.; Kaminski, M. D.; Chen, H.; Caviness, P. L.; Ebner, A. D.; Ritter, J. A. Magnetizable Implants and Functionalized Magnetic Carriers: A Novel Approach for Noninvasive yet Targeted Drug Delivery. *J. Magn. Magn. Mater.* **2005**, *293*, 633−638.

(9) Zanganeh, S.; Aieneravaie, M.; Erfanzadeh, M.; Ho, J.; Spitler, R. Magnetic Particle Imaging (MPI). *Iron Oxide Nanoparticles for Biomedical Applications*; Elsevier, 2018; pp 115−133.

(10) Kaul, M. G.; Weber, O.; Heinen, U.; Reitmeier, A.; Mummert, T.; Jung, C.; Raabe, N.; Knopp, T.; Ittrich, H.; Adam, G. *Combined Preclinical Magnetic Particle Imaging and Magnetic Resonance Imaging: Initial Results in Mice*; Georg Thieme Verlag KG, 2015; Vol. *187*, pp 347−352.

(11) Ferguson, R. M.; Khandhar, A. P.; Kemp, S. J.; Arami, H.; Saritas, E. U.; Croft, L. R.; Konkle, J.; Goodwill, P. W.; Halkola, A.; Rahmer, J.; Borgert, J.; Conolly, S. M.; Krishnan, K. M. Magnetic Particle Imaging with Tailored Iron Oxide Nanoparticle Tracers. *IEEE Trans. Med. Imaging* **2015**, *34*, 1077−1084.

(12) Arami, H.; Khandhar, A. P.; Tomitaka, A.; Yu, E.; Goodwill, P. W.; Conolly, S. M.; Krishnan, K. M. In Vivo Multimodal Magnetic Particle Imaging (MPI) with Tailored Magneto/Optical Contrast Agents. *Biomaterials* **2015**, *52*, 251−261.

(13) Panagiotopoulos, N.; Vogt, F.; Barkhausen, J.; Buzug, T. M.; Duschka, R. L.; Lüdtke-Buzug, K.; Ahlborg, M.; Bringout, G.; Debbeler, C.; Gräser, M.; Kaethner, C.; Stelzner, J.; Medimagh, H.; Haegele, J. Magnetic Particle Imaging: Current Developments and Future Directions. *Int. J. Nanomed.* **2015**, *10*, 3097.

(14) Venkatesha, N.; Poojar, P.; Qurishi, Y.; Geethanath, S.; Srivastava, C. Graphene Oxide-Fe3O4 Nanoparticle Composite with High Transverse Proton Relaxivity Value for Magnetic Resonance Imaging. *J. Appl. Phys.* **2015**, *117*, 154702.

(15) Cunningham, C. H.; Arai, T.; Yang, P. C.; McConnell, M. V.; Pauly, J. M.; Conolly, S. M. Positive Contrast Magnetic Resonance Imaging of Cells Labeled with Magnetic Nanoparticles. *Magn. Reson. Med.* **2005**, *53*, 999−1005.

(16) Wang, G.; Ma, Y.; Wei, Z.; Qi, M. Development of Multifunctional Cobalt Ferrite/Graphene Oxide Nanocomposites for Magnetic Resonance Imaging and Controlled Drug Delivery. *Chem. Eng. J.* **2016**, *289*, 150−160.

(17) Mohapatra, J.; Mitra, A.; Tyagi, H.; Bahadur, D.; Aslam, M. Iron Oxide Nanorods as High-Performance Magnetic Resonance Imaging Contrast Agents. *Nanoscale* **2015**, *7*, 9174−9184.

(18) Srivastava, P.; Sharma, P. K.; Muheem, A.; Warsi, M. H. Magnetic Nanoparticles: A Review on Stratagems of Fabrication and Its Biomedical Applications. *Recent Pat. Drug Deliv. Formulation* **2017**, *11*, 101−113.

(19) Shin, T.-H.; Choi, Y.; Kim, S.; Cheon, J. Recent Advances in Magnetic Nanoparticle-Based Multi-Modal Imaging. *Chem. Soc. Rev.* **2015**, *44*, 4501−4516.

(20) Terreno, E.; Castelli, D. D.; Viale, A.; Aime, S. Challenges for Molecular Magnetic Resonance Imaging. *Chem. Rev.* **2010**, *110*, 3019−3042.

(21) Saritas, E. U.; Goodwill, P. W.; Croft, L. R.; Konkle, J. J.; Lu, K.; Zheng, B.; Conolly, S. M. Magnetic Particle Imaging (MPI) for NMR and MRI Researchers. *J. Magn. Reson.* **2013**, *229*, 116−126.

(22) Wang, Y.; Wang, W.; Yu, L.; Tu, L.; Feng, Y.; Klein, T.; Wang, J.-P. Giant Magnetoresistive-Based Biosensing Probe Station System for Multiplex Protein Assays. *Biosens. Bioelectron.* **2015**, *70*, 61−68.

(23) Krishna, V. D.; Wu, K.; Perez, A. M.; Wang, J. P. Giant Magnetoresistance-Based Biosensor for Detection of Influenza A Virus. *Front. Microbiol.* **2016**, *7*, 400.

(24) Wu, K.; Klein, T.; Krishna, V. D.; Su, D.; Perez, A. M.; Wang, J.-P. Portable GMR Handheld Platform for the Detection of Influenza A Virus. *ACS Sens.* **2017**, *2*, 1594−1601.

(25) Tian, B.; de la Torre, T. Z. G.; Donolato, M.; Hansen, M. F.; Svedlindh, P.; Strömberg, M. Multi-Scale Magnetic Nanoparticle Based Optomagnetic Bioassay for Sensitive DNA and Bacteria Detection. *Anal. Methods* **2016**, *8*, 5009−5016.

(26) Wang, J.; Munir, A.; Zhu, Z.; Zhou, H. S. Magnetic Nanoparticle Enhanced Surface Plasmon Resonance Sensing and Its Application for the Ultrasensitive Detection of Magnetic Nanoparticle-Enriched Small Molecules. *Anal. Chem.* **2010**, *82*, 6782−6789.

(27) Bechstein, D. J. B.; Lee, J.-R.; Ooi, C. C.; Gani, A. W.; Kim, K.; Wilson, R. J.; Wang, S. X. High Performance Wash-Free Magnetic Bioassays through Microfluidically Enhanced Particle Specificity. *Sci. Rep.* **2015**, *5*, 11693.

(28) Wu, C. C.; Lin, L. Y.; Lin, L. C.; Huang, H. C.; Yang, Y. F.; Liu, Y. B.; Tsai, M. C.; Gao, Y. L.; Wang, W. C.; Hung, S. W.; Yang, S. Y.; Horng, H. E.; Yang, H. C.; Tseng, W. Y. I.; Yeh, H. I.; Hsuan, C. F.; Lee, T. L.; Tseng, W. K. Biofunctionalized Magnetic Nanoparticles for in Vitro Labeling and in Vivo Locating Specific Biomolecules. *Appl. Phys. Lett.* **2008**, *92*, 142504.

(29) Biederer, S.; Knopp, T.; Sattel, T. F.; Lüdtke-Buzug, K.; Gleich, B.; Weizenecker, J.; Borgert, J.; Buzug, T. M. Magnetization Response Spectroscopy of Superparamagnetic Nanoparticles for Magnetic Particle Imaging. *J. Phys. D Appl. Phys.* **2009**, *42*, 205007.

(30) Rauwerdink, A. M.; Weaver, J. B. Harmonic Phase Angle as a Concentration-Independent Measure of Nanoparticle Dynamics. *Med. Phys.* **2010**, *37*, 2587−2592.

DOI: 10.1021/acsami.9b05233
ACS Appl. Mater. Interfaces 2019, 11, 22979−22986

(31) Reeves, D. B.; Weizenecker, J.; Weaver, J. B. *Langevin Equation Simulation of Brownian Magnetic Nanoparticles with Experimental and Model Comparisons*; International Society for Optics and Photonics, 2013; Vol. *8672*, p 86721C.
(32) Deissler, R. J.; Wu, Y.; Martens, M. A. Dependence of Brownian and Néel Relaxation Times on Magnetic Field Strength. *Med. Phys.* **2014**, *41*, 012301.
(33) Deissler, R. J.; Martens, M. A. Dependence of the Magnetization Response on the Driving Field Amplitude for Magnetic Particle Imaging and Spectroscopy. *IEEE Trans. Magn.* **2015**, *51*, 1−4.
(34) Rauwerdink, A. M.; Giustini, A. J.; Weaver, J. B. Simultaneous Quantification of Multiple Magnetic Nanoparticles. *Nanotechnology* **2010**, *21*, 455101.
(35) Krause, H.-J.; Wolters, N.; Zhang, Y.; Offenhäusser, A.; Miethe, P.; Meyer, M. H. F.; Hartmann, M.; Keusgen, M. Magnetic Particle Detection by Frequency Mixing for Immunoassay Applications. *J. Magn. Magn. Mater.* **2007**, *311*, 436−444.
(36) Nikitin, P. I.; Vetoshko, P. M.; Ksenevich, T. I. New Type of Biosensor Based on Magnetic Nanoparticle Detection. *J. Magn. Magn. Mater.* **2007**, *311*, 445−449.
(37) Wu, K.; Schliep, K.; Zhang, X.; Liu, J.; Ma, B.; Wang, J.-P. Characterizing Physical Properties of Superparamagnetic Nanoparticles in Liquid Phase Using Brownian Relaxation. *Small* **2017**, *13*, 1604135.
(38) Wu, K.; Batra, A.; Jain, S.; Wang, J.-P. Magnetization Response Spectroscopy of Superparamagnetic Nanoparticles Under Mixing Frequency Fields. *IEEE Trans. Magn.* **2016**, *52*, 1−4.
(39) Liao, S.-H.; Yang, H.-C.; Horng, H.-E.; Yang, S. Y. Characterization of Magnetic Nanoparticles as Contrast Agents in Magnetic Resonance Imaging Using High-Tc Superconducting Quantum Interference Devices in Microtesla Magnetic Fields. *Supercond. Sci. Technol.* **2008**, *22*, 025003.
(40) Chieh, J. J.; Yang, S.-Y.; Horng, H.-E.; Yu, C. Y.; Lee, C. L.; Wu, H. L.; Hong, C.-Y.; Yang, H.-C. Immunomagnetic Reduction Assay Using High-T c Superconducting-Quantum-Interference-Device-Based Magnetosusceptometry. *J. Appl. Phys.* **2010**, *107*, 074903.
(41) Chen, M.-J.; Liao, S.-H.; Yang, H.-C.; Lee, H.-Y.; Liu, Y.-J.; Chen, H.-H.; Horng, H.-E.; Yang, S.-Y. Characterizing Longitudinal and Transverse Relaxation Rates of Ferrofluids in Microtesla Magnetic Fields. *J. Appl. Phys.* **2011**, *110*, 123911.
(42) Wu, K.; Yu, L.; Zheng, X.; Wang, Y.; Feng, Y.; Tu, L.; Wang, J.-P. *Viscosity Effect on the Brownian Relaxation Based Detection for Immunoassay Applications*; IEEE, 2014; pp 2769−2772.
(43) Wu, K.; Liu, J.; Wang, Y.; Ye, C.; Feng, Y.; Wang, J.-P. Superparamagnetic Nanoparticle-Based Viscosity Test. *Appl. Phys. Lett.* **2015**, *107*, 053701.
(44) Rauwerdink, A. M.; Hansen, E. W.; Weaver, J. B. Nanoparticle Temperature Estimation in Combined Ac and Dc Magnetic Fields. *Phys. Med. Biol.* **2009**, *54*, L51.
(45) Perreard, I. M.; Reeves, D. B.; Zhang, X.; Kuehlert, E.; Forauer, E. R.; Weaver, J. B. Temperature of the Magnetic Nanoparticle Microenvironment: Estimation from Relaxation Times. *Phys. Med. Biol.* **2014**, *59*, 1109.
(46) Tu, L.; Jing, Y.; Li, Y.; Wang, J.-P. Real-Time Measurement of Brownian Relaxation of Magnetic Nanoparticles by a Mixing-Frequency Method. *Appl. Phys. Lett.* **2011**, *98*, 213702.
(47) Gandhi, S.; Arami, H.; Krishnan, K. M. Detection of Cancer-Specific Proteases Using Magnetic Relaxation of Peptide-Conjugated Nanoparticles in Biological Environment. *Nano Lett.* **2016**, *16*, 3668−3674.
(48) Zhang, X.; Reeves, D. B.; Perreard, I. M.; Kett, W. C.; Griswold, K. E.; Gimi, B.; Weaver, J. B. Molecular Sensing with Magnetic Nanoparticles Using Magnetic Spectroscopy of Nanoparticle Brownian Motion. *Biosens. Bioelectron.* **2013**, *50*, 441−446.
(49) Orlov, A. V.; Khodakova, J. A.; Nikitin, M. P.; Shepelyakovskaya, A. O.; Brovko, F. A.; Laman, A. G.; Grishin, E. V.; Nikitin, P. I. Magnetic Immunoassay for Detection of Staphylococcal Toxins in Complex Media. *Anal. Chem.* **2013**, *85*, 1154−1163.
(50) Wu, K.; Su, D.; Saha, R.; Wong, D.; Wang, J.-P. Magnetic Particle Spectroscopy-Based Bioassays: Methods, Applications, Advances, and Future Opportunities. *J. Phys. D Appl. Phys.* **2019**, *52*, 173001.
(51) Hong, C.-Y.; Wu, C. C.; Chiu, Y. C.; Yang, S. Y.; Horng, H. E.; Yang, H. C. Magnetic Susceptibility Reduction Method for Magnetically Labeled Immunoassay. *Appl. Phys. Lett.* **2006**, *88*, 212512.
(52) Yang, C. C.; Yang, S. Y.; Chen, H. H.; Weng, W. L.; Horng, H. E.; Chieh, J. J.; Hong, C. Y.; Yang, H. C. Effect of Molecule-Particle Binding on the Reduction in the Mixed-Frequency Alternating Current Magnetic Susceptibility of Magnetic Bio-Reagents. *J. Appl. Phys.* **2012**, *112*, 024704.
(53) Hong, C.-Y.; Chen, W. S.; Jian, Z. F.; Yang, S. Y.; Horng, H. E.; Yang, L. C.; Yang, H. C. Wash-Free Immunomagnetic Detection for Serum through Magnetic Susceptibility Reduction. *Appl. Phys. Lett.* **2007**, *90*, 074105.
(54) Wu, K.; Wang, Y.; Feng, Y.; Yu, L.; Wang, J.-P. Colorize Magnetic Nanoparticles Using a Search Coil Based Testing Method. *J. Magn. Magn. Mater.* **2015**, *380*, 251−254.
(55) Tu, L.; Wu, K.; Klein, T.; Wang, J.-P. Magnetic Nanoparticles Colourization by a Mixing-Frequency Method. *J. Phys. D Appl. Phys.* **2014**, *47*, 155001.

DOI: 10.1021/acsami.9b05233
ACS Appl. Mater. Interfaces 2019, 11, 22979−22986